



## Performance characteristics in forward osmosis desalination modules containing membrane stiffeners

Ahmed M. Alshwairekh<sup>a,\*</sup>, Anas M. Alwatban<sup>a</sup>, Umar F. Alqsair<sup>b,c</sup>, Abdullah A. Alghafis<sup>a</sup>, Alparslan Oztekin<sup>c</sup>

<sup>a</sup>Mechanical Engineering Department, College of Engineering, Qassim University, Qassim 52571, Saudi Arabia, Tel. +966 16 380 0050 Ext. 5380; emails: shoierrk@qu.edu.sa (A.M. Alshwairekh), alwatban@qec.edu.sa (A.M. Alwatban), a.alghafis@qu.edu.sa (A.A. Alghafis)

<sup>b</sup>Mechanical Engineering Department, College of Engineering, Prince Sattam Bin Abdulaziz University, Alkharj 11942, Saudi Arabia, email: uma@lehigh.edu (U.F. Alqsair)

<sup>c</sup>P.C. Rossin College of Engineering and Applied Science, Lehigh University, PA 18015, USA, email: alo2@lehigh.edu (A. Oztekin)

Received 25 September 2019; Accepted 25 March 2020

---

### ABSTRACT

Computational fluid dynamics simulations are conducted on a forward osmosis desalination module consisting of the novel design of stiffener embedded membranes. The porous support layer has a negligible influence on the newly proposed forward osmosis membranes, and its effect of creating the internal concentration polarization is omitted. The design consisting of embedded stiffeners inside the membrane is introduced to mitigate the effect of the external concentration polarization. The embedded stiffeners also work as an added support for the membrane. Net-type stiffeners of 45° and various strand diameters are used for varying flow rates. A benchmark case with a flat membrane is used as a base to assess the performance of the stiffener embedded membrane modules. The laminar model is used for the geometry with the flat membrane, while  $k-\omega$  SST model is used to characterize the steady-state turbulent structures inside the forward osmosis desalination module containing stiffener embedded membranes. The mathematical model is validated using the existing experimental measurements in the literature. The results indicate that the embedded membrane with  $D = 0.3 h$  has alleviated the dilutive and concentrative external concentration polarization substantially and has increased the flux performance of more than 30%.

*Keywords:* Forward osmosis; Concentration polarization; Membranes; Embedded-stiffeners; Net-type stiffeners

---

### 1. Introduction

Freshwater resources are being depleted over time, and the water shortage is becoming a worldwide crisis. Water desalination by membranes offers a sustainable solution to overcome freshwater shortages. Decades ago, membrane systems emerged as a viable method to purify water. Depending on the type of the membrane and the separation driving force used in the systems, some membrane systems are categorized as: (1) reverse osmosis (RO),

(2) membrane distillation, and (3) forward osmosis (FO). In FO, the driving force is the osmotic pressure difference across the membrane caused by the concentration difference of the feed and the draw solutions.

To purify water using FO techniques, a suitable draw solution must be used, which possesses several important properties. Some of these properties are the solute must be easy to be separated from the draw solution in the next stage, chemically stable, non-toxic, and able to produce high osmotic pressures [1]. There were various draw solutions

---

\* Corresponding author.

developed by the researchers. With the different draw solutions proposed, different methods of water recovery at the second stage were also considered [2]. The focus of this work is on the first stage of the FO process. In water desalination applications using FO, the feed solution, which is the sea or brackish water, is introduced in the feed channel. The feed and draw channels are separated by a suitable semi-permeable membrane. The membranes used in FO systems are asymmetric in nature and consist of two parts, an active dense layer, and a thick porous support layer. The membrane could be oriented in any direction, depending on the application in hand. In water desalination, the active layer faces the feed solution to avoid the potential fouling that might occur inside the porous support layer. This orientation of the membrane is termed active layer facing feed solution (AL-FS) [3]. With the osmotic pressure difference across the semi-permeable membrane, pure water permeates from the feed channel to the draw channel. As water permeates to the draw channel, the concentration in the feed solution increases, and the concentration of the draw solution decreases. A concentration boundary layer starts to develop as a result of the water permeation. The water flux starts to decrease as the feed concentration increases and the draw concentration decreases near the membrane. The increase of the feed concentration near the membrane surface or the formation of a concentration boundary layer attached to the membrane surface at the feed side is termed concentrative external concentration polarization (CECP). The decrease in the draw concentration near the membrane surface is termed dilutive external concentration polarization (DECP).

A major disadvantage of FO desalination systems is the lack of suitable membranes. The membranes that are currently in use suffer from a severe internal concentration polarization (ICP). When the membrane is at the AL-FS orientation, a dilutive ICP occurs. Dilutive ICP cannot be mitigated by mixing since it happens inside the porous support layer. ICP phenomenon needs to be alleviated by a proper design applied to the fabrication phase of the membrane. In FO membranes, three main parameters affect the level of the ICP are thickness, porosity, and tortuosity of the porous support layer. The optimum solution for solving the ICP is to completely remove the porous support layer or make it as thin as possible. This option is an engineering challenge. The other options are to increase the porosity of the porous support layer and tailor the porous support layer pores so that the tortuosity is near unity. There are several attempts to manufacture improved FO membranes. Most of these attempts are in the research phase, and none of them reached a commercial phase. One of the well-known forward osmosis membranes is the one developed by Hydration Technologies Inc., (Oregon, USA). A detailed literature review of the developed membranes is presented in Table 1 by Qasim et al. [1].

The newly improved membranes still have a porous support layer. The effect of the ICP within newly proposed membranes is less severe than the previous membranes [4,5]. El Khaldi et al. [6] have fabricated a high-performance forward osmosis nanofiber-based substrate. The membrane is intended to be used for water desalination purposes. The resulted support layer is highly porous, and the reported water flux reached values up to 65 LMH. Marc et al. [7]

synthesized a nanofiber thin film composite membrane with a cross-linked electrospun polyvinyl alcohol nanofiber as a porous support layer. The structural parameter of the new membrane was low, but the water flux did not improve as much as compared to that achieved by the FO module of Song et al. [4]. Ghanbari et al. [8] developed a new membrane that has hydrophilic nanotubes inside the porous support layer. The membrane showed high water permeability and low reverse solute flux. Kuang et al. [9] used calcium carbonate nanoparticles to prepare the porous support layer. Hydrochloric acid was used to etch the calcium carbonate nanoparticles to increase the porosity of the support layer. Bui and Mccutcheon [10] fabricated a new membrane with incorporating mesoporous silica nanoparticles into the nanofiber porous support layer of the membrane. Their membrane showed remarkable flux increase, especially with pressure retarded osmosis (PRO) mode. Zheng et al. [11] have fabricated a new membrane by removing the polysulfone substrate from the ultrathin polyamide membrane and obtained water flux up to 80.54 LMH.

It is evident that the existence of the porous support layer hinders any advancement in FO and PRO systems due to ICP. Recently, Li et al. [12] developed a new membrane with only a dense active layer without the need for any support. The pure water permeability of the new membrane, however, was very low. If the techniques for synthesizing FO membranes advance in such manner, the ICP can be completely cured. However, the ECP is still an inherent phenomenon that will be present in any FO or PRO systems with any membrane. Several researchers indicate in their experimental work that spacers were placed within the feed, the draw, or both channels to enhance mixing and support the membrane. While this is true, the effect of using spacers might not just mix the feed or draw solutions. The lack of mixing might also lead to high fouling over the membrane surface in the feed channel [13,14]. Also, the existence of spacers adds extra pressure drop within the feed and draw channel which leads to more power consumption to operate such systems. Morrow and Childress [15] proposed that fouling mitigation strategies or mixing might be more promising than the fabrication of new membranes with enhanced properties.

In this work, the novel idea of a membrane-embedded stiffener design is introduced, and the flux performance of the proposed FO membrane and the polarization characteristics are explored using computational fluid dynamics simulations (CFD). The innovative membrane design

Table 1  
Area averaged concentrative external concentration polarization over the membrane at the feed side. Concentrative external concentration polarization values are determined for all geometries and flow rates considered

Re	Case			
	Flat	$D = 0.1 h$	$D = 0.2 h$	$D = 0.3 h$
300	1.7	1.61	1.48	1.41
800	1.51	1.38	1.27	1.23
1,500	1.41	1.23	1.18	1.15

aims to enhance mixing in the feed and draw channel with a minimal pressure drop. The unique design can also help in supporting the membrane, so the porous support layer is not needed. A net-type stiffener with various diameters will be embedded within the membrane structure.

## 2. Mathematical model and numerical method

### 2.1. Flow geometries

A schematic diagram for the embedded stiffener is shown in Fig. 1 with the side view (Fig. 1a) and the top view (Fig. 1b) of the embedded stiffener as it is inserted between two active layers of the membrane. Eight cells of the stiffener are included in the computational domain. The height of each channel is  $h$ , the width of the channels is  $5h$ , the length of the module is  $60h$ , and the angle between the horizontal and each strand of the stiffener is  $\theta = 45^\circ$ . The diameter of the stiffener strand is denoted as  $D$  in Fig. 1a. There are three geometries developed in this work that have the same dimension, as shown in Fig. 1a, except the stiffener's diameter. Three stiffener's diameters were considered as  $D = 0.1, 0.2,$  and  $0.3h$ . Simulations in each geometry were conducted for three flow rates corresponding to  $Re$  of 300; 800; and 1,500 using  $k-\omega$  SST turbulence model. Reynolds number is calculated as  $Re = (U_m \rho d_h) / \mu$ , where  $d_h = 2hw / (h + w)$  is the hydraulic diameter of the feed and draw a channel, and the width of each channel  $w = 5h$ . The flows near patterned surfaces are transitioned from the laminar to the turbulent regime for  $150 \leq Re \leq 500$  [19–21]. For  $Re = 300$ , we conducted simulations using both the laminar and turbulent flow model in FO membranes consisting of corrugated membranes and the channel walls [16]. We demonstrated that the flow and the concentration field, and the FO membrane performance obtained by the laminar and turbulence model are nearly identical.

The advantages of the embedded stiffeners used in the present study are (1) to enhance the flux performance of the module by inducing mixing in each channel, and (2) to strengthen the membrane. It is expected that the innovative

embedded stiffeners introduced here should yield better performance than both corrugated membrane and net type spacers placed inside each channel. The corrugated membrane provides an effective mixing at one side of the membrane, while the mixing will be induced equally effective at each side of the membrane in the embedded stiffeners geometry. The mixing induced by the net type spacers in both channels could be very effective, but spacers will cause a significant pressure drop in the system. The pressure drop caused by the embedded stiffeners will be very small since the mixing will be induced locally near the membrane surface where it is most needed and not in the bulk of each channel.

### 2.2. Governing equations and boundary conditions

The flow fields in the feed and the draw channels were modeled using the conservation of mass and momentum equations. The concentration distribution of the aqueous solution was modeled using the mass transport equation. The aqueous solution is assumed to be isothermal and incompressible. However, the density of the aqueous solution varies with the mass fraction. The conservation of mass is:

$$\frac{\partial}{\partial x_j} (\rho u_j) = 0 \quad (1)$$

The momentum equation is:

$$\rho u_j \frac{\partial u_i}{\partial x_j} = \frac{\partial}{\partial x_j} \left[ \mu \left( \frac{\partial u_i}{\partial x_j} + \frac{\partial u_j}{\partial x_i} \right) \right] - \frac{\partial p}{\partial x_i} \quad (2)$$

The mass transport equation is:

$$\rho u_j \frac{\partial c}{\partial x_j} = \frac{\partial}{\partial x_j} \left( \rho D_{AB} \frac{\partial c}{\partial x_j} \right) \quad (3)$$

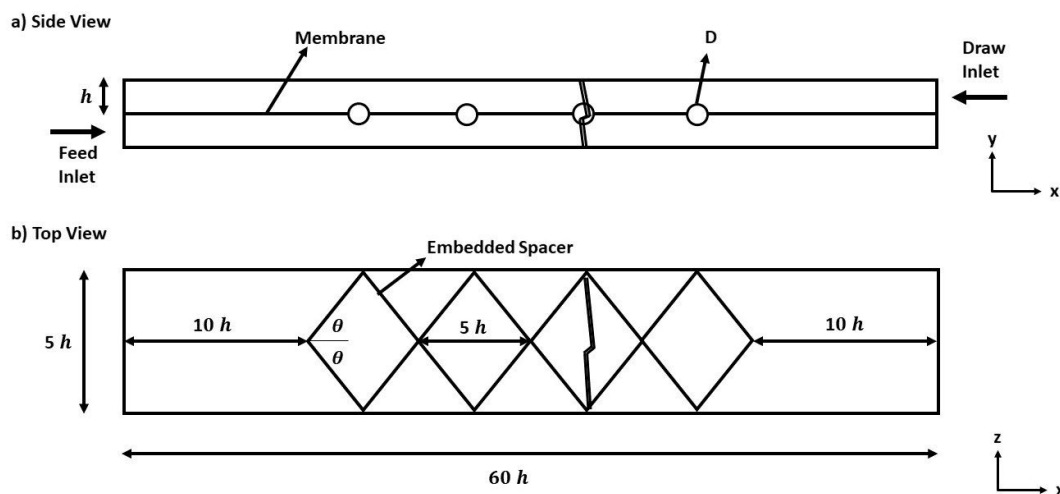


Fig. 1. Schematic diagram for the geometry (a) a side view showing both channels and (b) a top view showing the stiffener arrangement.

where  $\rho$  is density,  $\mu$  is viscosity,  $c$  is the solute mass fraction,  $D_{AB}$  is the solute diffusion coefficient,  $p$  is the pressure, and  $u_i$  is the velocity vector,  $i$  and  $j$  are tensorial indices. The flow and physical parameters displayed denote properties of the feed and draw solution stream. The temperature of the aqueous solution, taken to be constant at 25°C, might play an important role in improving the FO systems. Sodium chloride (NaCl) is considered as a solute in the feed and draw solution with a range of concentration to model the seawater desalination. The properties of the NaCl and Na<sub>2</sub>SO<sub>4</sub> solution at 25°C as a function of a mass fraction are given as [17]:

$$\begin{aligned} \rho &= 997.1 + 694c && [\text{NaCl}] \\ \rho &= 997.1 + 909c && [\text{Na}_2\text{SO}_4] \end{aligned} \quad (4)$$

$$\begin{aligned} \mu &= 0.89 \times 10^{-3} (1 + 1.63c) && [\text{NaCl}] \\ \mu &= 0.89 \times 10^{-3} (1 + 3.52c) && [\text{Na}_2\text{SO}_4] \end{aligned} \quad (5)$$

$$\begin{aligned} D_{AB} &= \begin{cases} 1.61 \times 10^{-9} (1 - 14c) & \text{for } c < 0.006 \\ 1.45 \times 10^{-9} & \text{for } c > 0.006 \end{cases} && [\text{NaCl}] \\ D_{AB} &= 1.23 (1 - 0.76c^{0.4}) && [\text{Na}_2\text{SO}_4] \end{aligned} \quad (6)$$

The Na<sub>2</sub>SO<sub>4</sub> solution is used in the validation study.

Several researchers [18–22] conducted CFD simulations in membrane systems containing turbulence promoters using the turbulent model  $k$ – $\omega$  shear stress transport (SST). We employed the  $k$ – $\omega$  SST turbulence model to characterize the steady-state turbulent structures induced by the presence of the embedded stiffeners [23–25]. The SST  $k$ – $\omega$  turbulence momentum equation is written as:

$$\rho \bar{u}_j \frac{\partial \bar{u}_i}{\partial x_j} = \frac{\partial}{\partial x_j} \left[ (\mu + \mu_t) \left( \frac{\partial \bar{u}_i}{\partial x_j} + \frac{\partial \bar{u}_j}{\partial x_i} \right) \right] - \frac{\partial \bar{p}}{\partial x_i} \quad (7)$$

The turbulence mass transport equation is:

$$\rho \bar{u}_j \frac{\partial \bar{c}}{\partial x_j} = \frac{\partial}{\partial x_j} \left[ \rho (D_{AB} + D_t) \frac{\partial \bar{c}}{\partial x_j} \right] \quad (8)$$

where  $\bar{u}_i$  and  $\bar{c}$  are the time-averaged (filtered) velocity and concentration,  $\bar{p}$  is the resolved pressure,  $\mu_t = \rho \frac{a_1 k}{\max(a_1 \omega, S_{\tau}^2)}$  is the eddy viscosity,  $D_t = \frac{\mu_t}{\rho S_{\tau}}$  is the eddy diffusion coefficient, and  $S_{\tau}$  is the turbulent Schmidt number. The turbulent Schmidt number is selected to be 0.85, and the Schmidt number for fluid,  $S_c = \frac{\mu_t}{\rho D_{AB}}$ , is set to 667. The turbulent kinetic energy  $k$  and the specific dissipation rate  $\omega$  are given as:

$$\rho \bar{u}_j \frac{\partial k}{\partial x_j} = \tau_{ij} \frac{\partial \bar{u}_i}{\partial x_j} - \beta^* \rho \omega k + \frac{\partial}{\partial x_j} \left[ (\mu + \sigma_{k1} \mu_t) \frac{\partial k}{\partial x_j} \right] \quad (9)$$

$$\begin{aligned} \rho \bar{u}_j \frac{\partial \omega}{\partial x_j} &= \frac{\gamma}{\nu_t} \tau_{ij} \frac{\partial \bar{u}_i}{\partial x_j} - \beta \rho \omega^2 + \frac{\partial}{\partial x_j} \left[ (\mu + \sigma_{\omega} \mu_t) \frac{\partial \omega}{\partial x_j} \right] \\ &+ 2\rho (1 - F_1) \sigma_{\omega 2} \frac{1}{\omega} \frac{\partial k}{\partial x_j} \frac{\partial \omega}{\partial x_j} \end{aligned} \quad (10)$$

The model parameters and the constants that appeared in Eqs. (7)–(10) are given in full detail in Menter [26]. Also,  $S$  is the vorticity magnitude and  $(a_1, \beta, \beta^*, \sigma_{k1}, \sigma_{\omega}, \sigma_{\omega 2}, \text{ and } \gamma)$ ,  $(F_1, F_2)$  are closure coefficients and blending functions, respectively.

In FO membrane systems, the water flux can be modeled using the solution–diffusion model [27] as:

$$J_w = A (\pi_{d,m} - \pi_{f,m}) \quad (11)$$

where  $A$  is the pure water permeability of the membrane.  $\pi_{d,m}$  and  $\pi_{f,m}$  are the osmotic pressures across the semi-permeable membrane calculated at the membrane interface at the draw and feed side, respectively. The value of the pure water permeability can be obtained using a pressure-driven test [28]. The osmotic pressure along the membrane at the feed and draw side can be estimated using the empirical relations depending on the solution used [17].

$$\begin{aligned} \pi &= 805.1 \times 10^5 c && [\text{for NaCl}] \\ \pi &= 337.8 \times 10^5 c^{0.95} && [\text{for Na}_2\text{SO}_4] \end{aligned} \quad (12)$$

To model the water flux for FO membranes with the presence of the porous support layer Eq. (11) cannot be used. A modified version of the solution–diffusion model is used where the presence of the porous support layer is given via a diffusion resistivity coefficient as [29]:

$$J_w = \frac{1}{K} \ln \left( \frac{B + A \pi_{d,i}}{B + |J_w| + A \pi_{f,m}} \right) \quad (13)$$

In the Eq. (13),  $B$  is the solute permeation coefficient,  $K$  is the diffusion resistivity coefficient given as:

$$K = \frac{t_s \tau}{D_{AB} \varepsilon}, \quad S = K D_{AB} = \frac{t_s \tau}{\varepsilon} \quad (14)$$

where  $S$  is the membrane structural parameter,  $t_s$  is the porous support layer thickness,  $\varepsilon$  is the porosity, and  $\tau$  is the tortuosity of the pores in the porous layer. The structural parameter increases with increasing thickness and decreasing porosity. It also increases as tortuosity increases. The increasing tortuosity denotes the randomness of the pore structures. As pores are aligned (low tortuosity), the stiffness of the membrane decreases. The structural parameter is inversely proportional to permeability.

The solute in the draw solution can sweep into the feed channel, which is undesirable, and it is termed as the solute reverse flux which can be modeled using the solution–diffusion equation as [29]:

$$J_s = -\frac{B}{\varnothing \cdot A} J_w \quad (15)$$

In Eq. (15), the proportionality factor  $\varnothing = 805 \times 10^2 \text{ Pa m}^3 \text{ kg}^{-1}$ . The negative sign indicates that the solute flux is opposing the water flux. It is desired to have a low solute permeation coefficient and a high-water permeability coefficient. The solute permeation coefficient is estimated using:

$$B = \frac{1-R}{R} |J_w| \quad (16)$$

where,  $R$  is the salt rejection coefficient, and  $B$  is approximated as constant with the value of  $1.42 \times 10^{-6} \text{ m s}^{-1}$ .

The boundary conditions at the inlet of both the feed and draw channel used in the simulations are  $\bar{c} = c_{in}$ ,  $\bar{u} = 6U_{in} \frac{y}{h} \left(1 - \frac{y}{h}\right)$ ,  $\bar{v} = 0$ ,  $\bar{w} = 0$ . Here,  $U_{in}$  is the average inlet velocity,  $y$  is the vertical distance from the bottom of the feed channel,  $u$ ,  $v$ , and  $w$  are the components of the velocity, and  $h$  is the height of either the feed or draw channel. For water to permeate from the feed to draw channel, the inlet concentration of the feed must be lower than the draw solution.

The boundary conditions imposed at the channel walls and the surface of embedded stiffeners are no-slip, no penetration, and  $\frac{\partial \bar{c}}{\partial y} = 0$ .

The boundary conditions of the membrane at each side are:

$$-\rho D_{AB} \frac{\partial \bar{c}}{\partial y} + \rho \bar{c} \bar{J}_w = J_s, \bar{v} = J_w = A(\pi_{d,m} - \pi_{f,m}), \bar{u} = 0, \text{ and } \bar{w} = 0 \quad (17)$$

Note that the suction velocity could have been replaced by Eq. (13) if the effect of the porous layer is to be included. The periodic boundary conditions are applied at the sidewalls,  $z/h = 0$  and  $5$ .

### 2.3. Numerical method and mesh study

The pure water permeability of the membrane used in the simulations was taken from the membrane developed by Liang et al. [5], and it is estimated to be  $4.71 \pm 0.22 \text{ L m}^{-2} \text{ h}^{-1} \text{ bar}^{-1}$ . In their work, they have reduced the effect of the porous support layer drastically by tailoring the orientation of the porous pores in a cylindrical manner. Therefore, based on the stated literature review, the effect of the porous layer in our model was neglected. The osmotic transmembrane pressure  $\Delta\pi$  was set to 2 MPa by using a brackish water of 0.004 solute mass fraction (4,000 ppm) and a draw solution of solute mass fraction equivalent to 0.0288 (28,800 ppm).

The governing equations were coupled and solved by utilizing a UDF to define a new transport equation for the solute concentration. The flux model, along with the boundary conditions, was also defined using the UDF. A second-order upwind scheme was used for the governing

equations with the SIMPLE scheme. The absolute residual convergence criteria of  $10^{-3}$  was applied. The CFD model was implemented in Ansys Fluent 17.1. The computational domain was discretized using the unstructured tetrahedral elements. An inflation layer near the membrane was used to capture the external concentration polarization that happens in both channels, with the first layer thickness of the inflation layer was  $5 \mu\text{m}$  [30]. The mesh optimization test was conducted to ensure the predicted flow and concentration field, and the membrane flux performance is independent of the mesh density selected. The case with  $D = 0.3 h$  and  $\text{Re} = 1,500$  was used in the optimization test. Three mesh densities M1, M2, and M3, were utilized corresponding to a total number of cells as 10, 20, and 40 million, respectively. Fig. 2 shows the profiles of the stream-wise velocity in the feed channel and concentrations along the membrane surface at the feed and draw side at  $z/h = 2.5$  obtained using the three different mesh density. The concentration profiles at each side of the membrane obtained by three mesh density are nearly the same with some deviations at the peak values. The level of deviation in the peak values of the concentration predicted by M2 and M3 is small, as shown in Figs. 2a and c. The profiles of the stream-wise velocity in the feed channel at  $y/h = 0.5$  and  $z/h = 2.5$  obtained by the mesh density M2 and M3 are nearly the same. The concentration profile in the feed channel at  $z/h = 2.5$  predicted by M1, M2, and M3 are nearly identical, as shown in Fig. 2d. The results of the mesh independence test reveal that the mesh density of 20 million elements is sufficient to ensure the spatial convergence of the velocity and concentration field in the FO module. Results presented in this study were acquired using 20 million elements. A section of the used mesh is shown in Fig. 3.

### 3. Results

A validation study is conducted using the experimental setup of Li et al. [12]. In their experiments, the newly developed membrane excluded the porous support layer had only an active layer present. The pure water permeability coefficient for the membrane with a thickness of  $5 \mu\text{m}$  was estimated to be  $0.16 \text{ L m}^{-2} \text{ h}^{-1} \text{ bar}^{-1}$ . The validation study was conducted in a cell with known dimensions of  $78 \text{ mm} \times 25 \text{ mm} \times 5 \text{ mm}$ . The feed and the draw solutions used were comprised of deionized water and  $\text{Na}_2\text{SO}_4$  with different concentrations, respectively. The average velocity of the solutions in the test cell was set to  $10.36 \text{ cm s}^{-1}$  which corresponds to  $\text{Re}$  of 860. The flow in the module without stiffeners is laminar. The same Reynolds number was used in the CFD simulations to match the same flow and concentration field of the experiment. The draw concentration in the experiment was varied from 0.4 to  $1.5 \text{ mol L}^{-1}$  of  $\text{Na}_2\text{SO}_4$  with the deionized water in the feed channel. The concentration of the draw solution in the validation simulations was taken as  $0.5 \text{ mol L}^{-1}$  since the relations given in the mathematical model for the physical properties of  $\text{Na}_2\text{SO}_4$  are valid only for a mass fraction of less than or equal to 0.09. The predicted water flux is  $4 \text{ kg m}^{-2} \text{ h}^{-1}$  while the reported water flux by Li et al. [12] is  $4.35 \text{ kg m}^{-2} \text{ h}^{-1}$  under the same conditions. The predicted and measured reverse solute flux are  $2.88$  and  $3 \text{ g m}^{-2} \text{ h}^{-1}$ , respectively. The variation between the predictions and

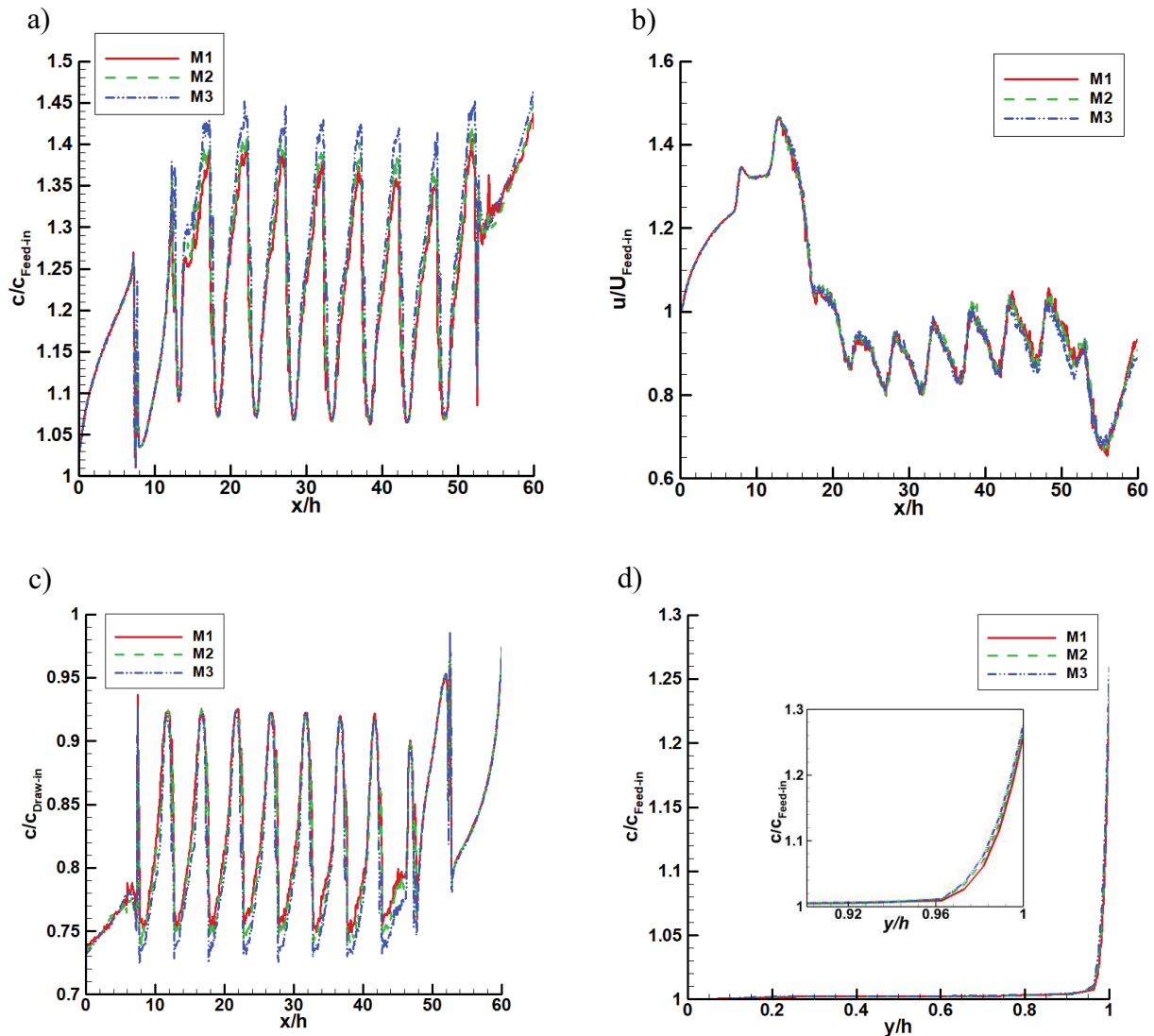


Fig. 2. Profiles in the stream-wise direction of (a) the normalized concentration on the membrane in the feed channel at  $z/h = 2.5$ , (b) the normalized stream-wise velocity in the feed channel at  $y/h = 0.5$  and  $z/h = 2.5$ , and (c) the normalized concentration along the membrane in the draw channel at  $z/h = 2.5$ . (d) The profiles of the normalized concentration in the feed channel at  $x/h = 25$  and  $z/h = 2.5$ . The inset in Fig. 2d shows the profile near the membrane surface for  $y/h = 0.9$  to  $y/h = 1$ . Profiles obtained using the mesh density of M1, M2, and M3.

measurements in the water flux and the reverse solute flux are 9% and 4%, respectively. The agreement with our results and experiments validate the mathematical model and numerical methods employed. It should be noted that both flux equations were used, that is, Eqs. (11) and (13) in the validation study and the water flux predicted is similar. We employed Eq. (11) in determining the water flux through the membrane since the effect of the porous layer is negligible.

It would be preferred to conduct the validation study in a module containing a membrane with embedded stiffeners. The authors did not have the resources to conduct an experimental study. It would also be desirable to compare our predictions of concentration distribution over the membrane surface against experimental measurements. That would

validate the mathematical model and numerical method more convincingly.

Contours of the normalized stream-wise velocity for  $Re = 300, 800, \text{ and } 1,500$  are shown in Fig. 4 for  $D = 0.1, 0.2, \text{ and } 0.3 h$ . The velocity contours normalized with the average inlet velocity are rendered in the middle of the feed channel at  $y/h = 0.5$  and  $22.5 < x/h < 47.5$ . For  $D = 0.1 h$ , it is observed that nearly all the contours follow a similar trend. The stream-wise velocity contours resemble a velocity contour for an empty channel. Faded high-velocity regions are observed in the flow channel that takes the shape of the embedded stiffener. This trend is observed for all flow rates. The velocity field for  $D = 0.2$  and  $0.3 h$  at  $Re = 300$  is similar to that of  $D = 0.1 h$  at the same Reynolds number. The only difference is that the stiffeners' signature is more pronounced in

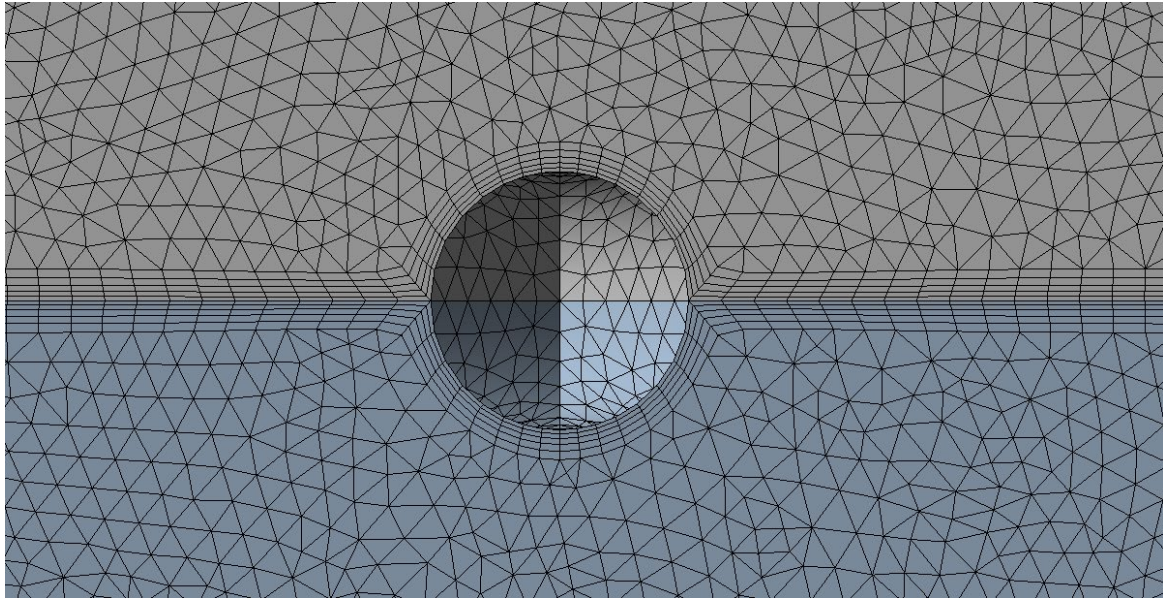


Fig. 3. Section of the mesh used that shows the inflation layer near the membrane with the embedded stiffener.

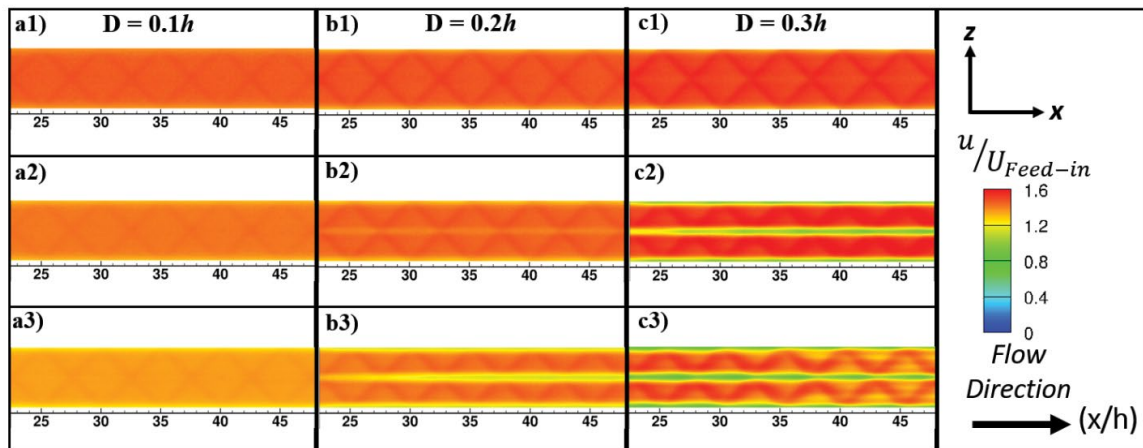


Fig. 4. Contours of normalized stream-wise velocity in the middle of the feed channel for  $Re = 300$  (a1, b1, c1),  $Re = 800$  (a2, b2, c2), and  $Re = 1,500$  (a3, b3, c3). Flow images are rendered in the module containing membrane with embedded stiffeners of strand diameter  $D = 0.1 h$  (a1, a2, a3),  $D = 0.2 h$  (b1, b2, b3), and  $D = 0.3 h$  (c1, c2, c3).

$D = 0.2$  and  $0.3 h$ . For  $Re = 800$ , the velocity contours show different characteristics for the larger diameter of the stiffener strand. There is a distinct horizontal low-velocity region that cuts in the middle of the channel. The contour has divided into two distinct regions in each set of stiffeners. The high-velocity region is divided into two regions, and this division is made by a distinct low-velocity region that crosses the intersections of strands. The intensity of this low-velocity region in the middle is heightened in  $Re = 1,500$ . Also, the same low-velocity region can be seen at  $z/h = 0$  and  $5$  which is a region of strands intersection. The flow field for  $D = 0.3 h$  shares similar characteristics with more distinct imprints of the stiffeners on the contours which corresponds to high-velocity regions. The flow is considered hydrodynamically developed since there is a clear, repeated structure in the

contours. The stream-wise velocity in the middle of the draw channel for the same flow rate has the same trend for the feed channel since the embedded stiffeners orientation is the same at both sides of the membrane.

Iso-surfaces of  $Q$ -criterion for  $Re = 300$ ;  $800$ ;  $1,500$  and  $D = 0.1, 0.2$ , and  $0.3 h$  are depicted in Fig. 5 iso-surfaces are colored with the vorticity in each geometry. The  $Q$ -criterion is the second invariant of the velocity gradient tensor and can reveal the turbulent flow structures induced by the presence of the embedded stiffeners within the membrane.  $Q$ -criterion is determined as  $Q = -0.5 \left( \|S_{ij}\|^2 - \|\Omega_{ij}\|^2 \right)$ , where the symmetric rate of the strain tensor  $S_{ij} = 0.5 \left[ \frac{\partial u_i}{\partial x_j} + \left( \frac{\partial u_j}{\partial x_i} \right)^T \right]$ , and the

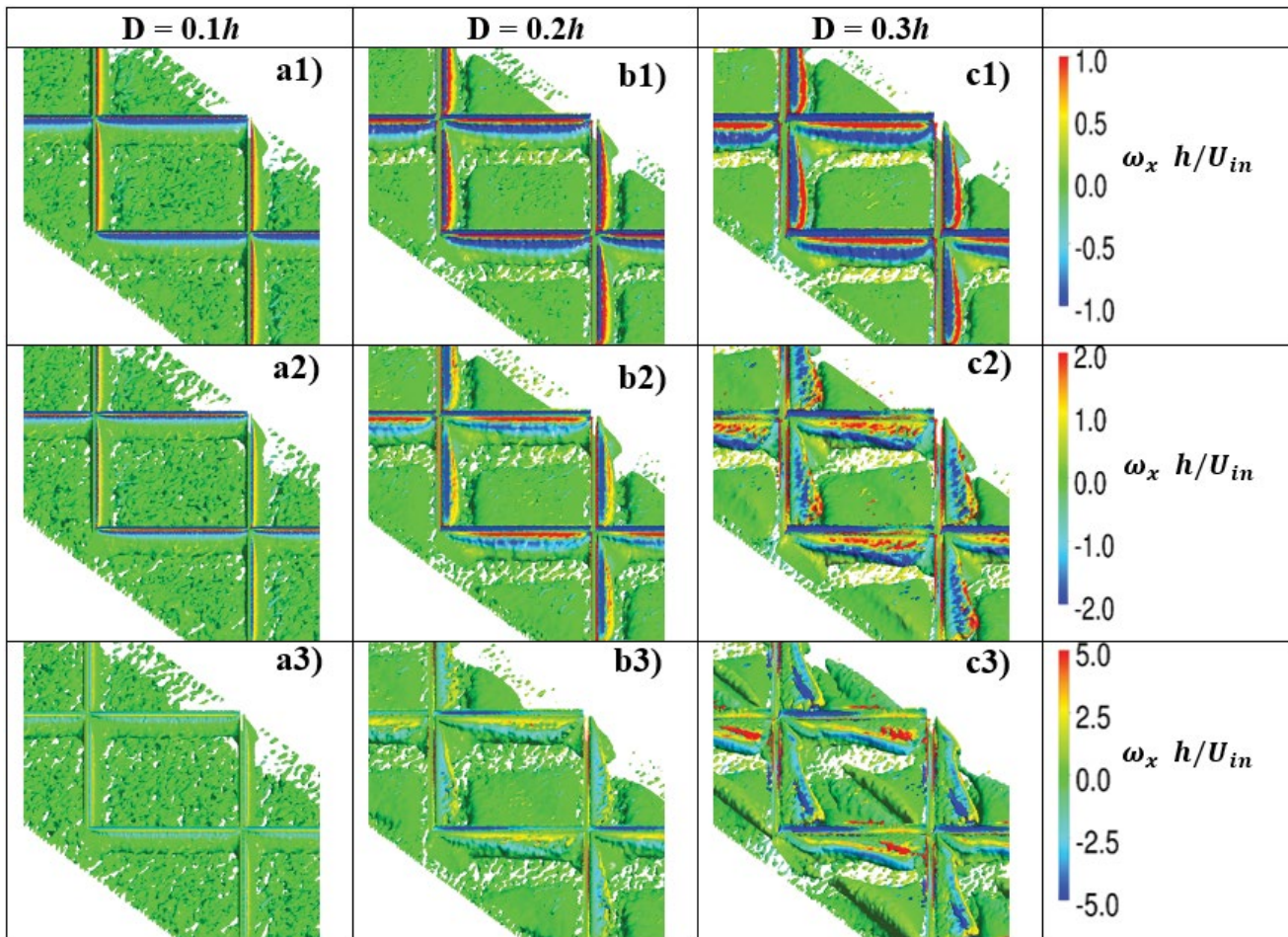


Fig. 5. Iso-surfaces of the normalized  $Q$ -criterion at a level 0.01 plotted in the feed channel for  $Re = 300$  (a1, b1, c1),  $Re = 800$  (a2, b2, c2), and  $Re = 1500$  (a3, b3, c3). Flow images are rendered in the module containing membrane with embedded stiffeners of strand diameter  $D = 0.1 h$  (a1, a2, a3),  $D = 0.2 h$  (b1, b2, b3), and  $D = 0.3 h$  (c1, c2, c3). The iso-surfaces are colored with the normalized vorticity.

$$\text{antisymmetric rate of rotation tensor } \Omega_{ij} = 0.5 \left[ \frac{\partial u_i}{\partial x_j} - \left( \frac{\partial u_j}{\partial x_i} \right)^T \right]$$

The vortical activities increase as the flow rate increases for the fixed strand diameter, and it also increases as the strand diameter increases for the fixed flow rate, as shown in Fig. 5. The vortical activities are strongest in the downstream vicinity of strands. At low flow rates, the vortices generated from strands dissipate rapidly, and the region inside the cells is lack of vortical activities. At the higher flow rates, the vortices generated from the strands and the channel wall become stronger and penetrate the central region of the cells. The intense vortical activities induce enhanced mixing and aid in mitigating external concentration polarization at each side of the membrane. The embedded stiffener with the larger diameter generates better mixing near the membrane surface at all flow rates and is desirable for better performance of the FO module. For small strand diameter at all flow rates, highly populated small scale, low-intensity vortices generated away from the membrane, but they don't help to mitigate the concentration polarization in the module.

Fig. 6 shows the normalized concentration contours along the membrane surface at the feed side for  $Re = 300$ ; 800; 1,500 and  $D = 0.1, 0.2$ , and  $0.3 h$ . The contours are normalized with the inlet feed concentration. Since the embedded stiffeners are modeled as impermeable surfaces, images are not rendered in these regions, which are denoted by white areas in the contours over the membrane surface. Figs. 6a1–a3 shows the concentration contours for  $D = 0.1 h$  and  $Re = 300, 800$ , and  $1,500$ , respectively. There is a high-level concentrative CP on the membrane surface at  $Re = 300$ . The region over the membrane surface between each successive intersection of the strands shows a distinct high concentrative CP area. The salt concentration decreases away from the intersection region at each side. The concentration polarization level decreases significantly as the flow rate is increased to  $Re = 800$  and  $1,500$ . The increase in stiffeners strand diameter shows an improvement to the level of concentrative concentration polarization over the membrane surface. The extremely high concentration levels seen in  $D = 0.1 h$  for  $Re = 300$  have been lowered with increasing the strand diameter by an increment of  $0.1 h$  as seen in Fig. 5b1 for  $D = 0.2 h$ . For  $Re = 800$  and  $1,500$ ,

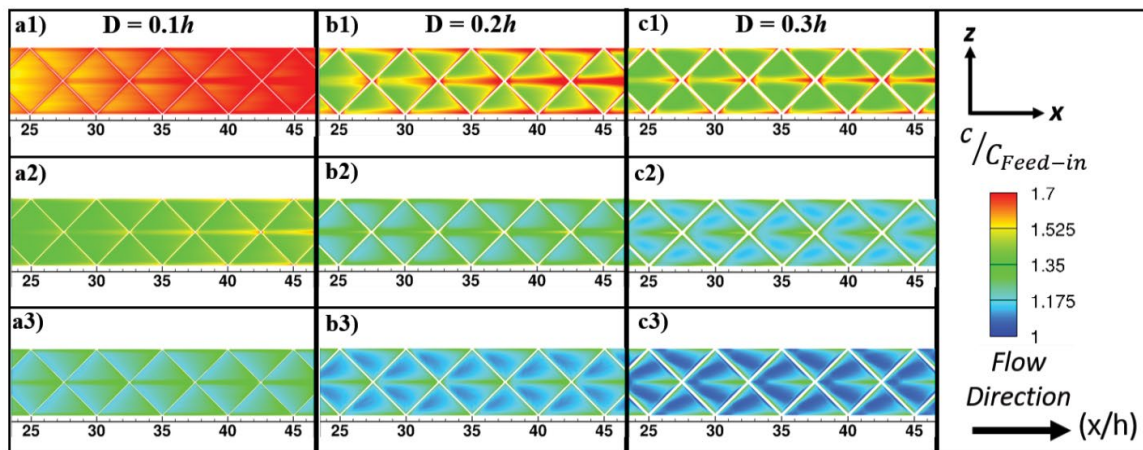


Fig. 6. Normalized contours of the external concentrative CP for  $Re = 300$  (a1, b1, c1),  $Re = 800$  (a2, b2, c2), and  $Re = 1,500$  (a3, b3, c3). Images are rendered in the module containing membrane with embedded stiffeners of strand diameter  $D = 0.1 h$  (a1, a2, a3),  $D = 0.2 h$  (b1, b2, b3), and  $D = 0.3 h$  (c1, c2, c3).

the concentration shows similar trends as in  $D = 0.1 h$  module with a significantly lowered concentration polarization level, as illustrated in Figs. 6b2 and b3. The membrane with  $D = 0.3 h$  is performing much better regarding mitigating the concentration polarization. The vorticity field depicted in Fig. 5 indicated that mixing in the geometry with  $D = 0.3 h$  is profoundly greater than the other two geometries. For  $Re = 300$ , the middle line crossing the region inside the cell where strands intersect shows a high concentration area. This line is dividing the membrane surface to two low concentration regions away from the center. For  $Re = 800$ , a similar trend is observed. However, the line that divides the membrane is thinner, and it almost disappears. As for  $Re = 1,500$ , this line is the same compared with  $Re = 800$ . However, the concentration polarization is lower in the two regions next to the dividing line. In all geometries and for all flow rates, the region around the dividing line has the highest CP level since this area of the membrane experience the lowest vortical activities (Fig. 5). Table 1 shows a summary of the area-averaged concentration polarization over the membrane at the feed side for all flow rates considered. The concentrative concentration polarization is mitigated in the FO module containing embedded stiffeners. The level of polarization decreases as the strand diameter is increased at a fixed flow rate. The polarization mitigation has increased profoundly with an increased flow rate for each size strand.

Fig. 7 presents the local variation of the concentration in the feed channel over the membrane surface at  $z/h = 1.25$  for  $Re = 1,500$  and  $D = 0.1, 0.2$ , and  $0.3 h$ . In Figs. 7a–c the concentration profiles are depicted in the stream-wise direction from the inlet to the outlet of the feed channel. The feed concentration over the membrane surface increases in the stream-wise direction since there is a mass transfer of water to the draw channel. In the module containing flat membranes, the concentration boundary layer grows in the stream-wise direction since there is a lack of flow-induced mixing, as depicted in Fig. 7. In the module containing embedded stiffeners, however, a flow-induced mixing resulted from the presence of stiffeners disrupts the

growth of the concentration boundary layer and suppresses the increase of concentration over the surface of the membrane. The peaks and valleys are observed in the profiles with repeated patterns following the cells of embedded stiffeners. The nominal value of the concentration decreases as  $Re$  is increased. It is demonstrated here that the presence of the embedded-stiffeners alleviates the concentrative concentration polarization at the feed side as it is attributed to the enhanced local flow-induced mixing near the membrane surface.

Figs. 8a–c show the contours of the normalized concentration in the draw channel for  $Re = 300$ ; 800; and 1,500 in the geometries for  $D = 0.1, 0.2$ , and  $0.3 h$ . Since the flow in the draw channel is similar to the flow in the feed channel, the concentration contours are also similar to the contours in the feed channel. The important difference is that having a higher concentration over the membrane surface in the draw side is favorable. Also, there is no risk of fouling on the membrane surface in the draw side. The average dilutive CP for the cases of  $Re = 300$ ; 800; and 1,500 are 0.69, 0.76, and 0.82 for the membrane with  $D = 0.1 h$ , respectively. Therefore, increasing the flow rate in the draw channel decreases the intensity of the dilutive CP as it is approaching the unity. For  $Re = 300$ , the low concentration regions tend to be in the stiffener's cells and away from the center. For  $Re = 800$ , the distribution of the concentration is almost constant, and fading regions of low concentration are observed in the middle of the stiffener's cells. For  $Re = 1,500$ , the high concentration regions are much clearer, and they tend to be inside the stiffener's cell and behind the stiffener strand in the direction of the flow. A similar trend is seen in modules with  $D = 0.2$  and  $0.3 h$ , as depicted in Fig. 8. Table 2 shows the average dilutive concentration polarization for the membrane in the draw channel. The dilutive concentration is mitigated slightly better as the stiffener strand's diameter is increased. The polarization level decreases significantly as the flow rate is increased with any size strand. Also, increasing the flow rate reduces the level of concentration polarization [31].

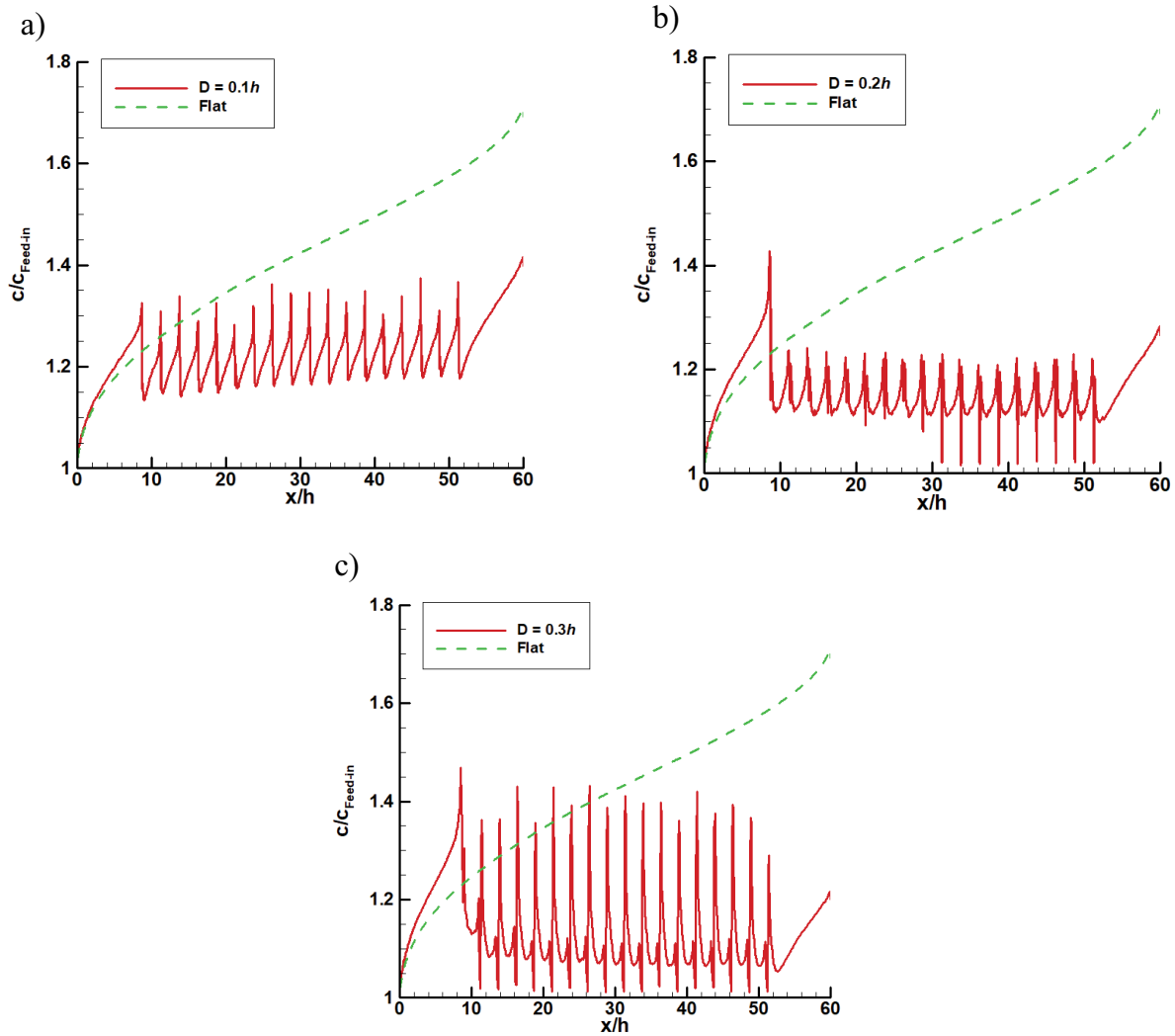


Fig. 7. Profiles of the normalized concentration on the membrane surface at the feed side at  $z/h = 2.5$  for  $Re = 1,500$ . Concentration profiles are acquired in the module containing embedded stiffeners of strand diameter (a)  $D = 0.1 h$ , (b)  $D = 0.2 h$ , and (c)  $D = 0.3 h$  and are compared to that obtained in the module containing membrane without the embedded stiffeners.

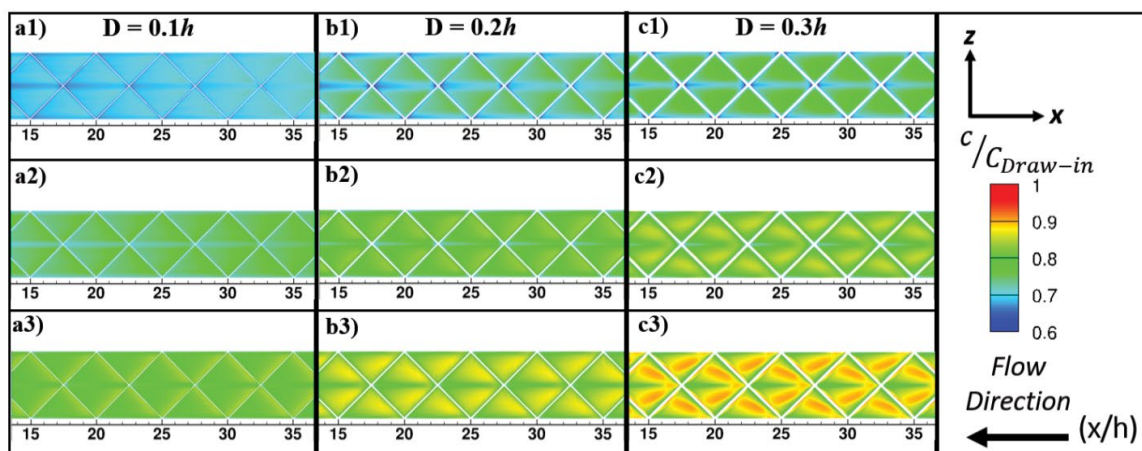


Fig. 8. Normalized contours of the external dilutive CP for  $Re = 300$  (a1, b1, c1),  $Re = 800$  (a2, b2, c2), and  $Re = 1,500$  (a3, b3, c3). Images are rendered in the module containing membrane with embedded stiffeners of strand diameter  $D = 0.1 h$  (a1, a2, a3),  $D = 0.2 h$  (b1, b2, b3), and  $D = 0.3 h$  (c1, c2, c3).

Table 2

Area averaged dilutive external concentration polarization over the membrane at the draw side. Dilutive external concentration polarization values are determined for all geometries and flow rates considered

Re	Case			
	Flat	$D = 0.1 h$	$D = 0.2 h$	$D = 0.3 h$
300	0.67	0.69	0.73	0.75
800	0.71	0.76	0.80	0.82
1,500	0.74	0.82	0.85	0.87

Figs. 9a–c show the normalized wall shear stress over the surface of the membrane at the feed side for  $Re = 300$ , 800, and 1,500, and  $D = 0.1, 0.2$ , and  $0.3 h$ . The shear stress is normalized with the maximum value obtained along the surface of the membrane for each geometry and flow rate. Shear stress plays an important role in assessing membrane performance as it is a measure of the propensity of fouling over the membrane surface. Regions of low shear stress are more prone to fouling. For a small stiffener strand diameter, the shear stress distribution over the membrane surface is similar to that over the membrane without the embedded stiffeners. Only the region near the strands has a low value of shear stress. As the flow rate is increased, the regions of low shear stress near the strands develop larger. In the modules with  $D = 0.2$  and  $0.3 h$ , the variation of the wall shear stress over the surface becomes wider. As the flow rate is increased, two distinct high shear stress regions are observed within each cell. Behind the intersection of strands, there is a low shear stress region. Table 3 shows the maximum shear stress values over the feed membrane. As  $Re$  is increased, the maximum wall shear stress increases in all three geometries. Also, as  $D$  increases the maximum value of the wall shear stress increases and the increase is nearly two-fold at the high flow rate. The module with  $D = 0.3 h$  at the high flow rate,  $Re = 1,500$ , is much less likely to have fouling over the membrane surface.

Table 3

Maximum shear stress values over the membrane surface at the feed side – all values are in the unit of Pa. The wall shear stress values are determined for all geometries and flow rates considered

Re	Case			
	Flat	$D = 0.1 h$	$D = 0.2 h$	$D = 0.3 h$
300	1.04	1.05	1.07	1.09
800	2.77	3	3.1	3.49
1,500	5.47	6.75	7.1	12.5

Figs. 10a–c shows the normalized local water flux over the membrane surface for  $Re = 300, 800$ , and  $1,500$ , and  $D = 0.1, 0.2$ , and  $0.3 h$ . The water flux is normalized with the pure water permeability and the osmotic transmembrane pressure. For  $Re = 300$ , the water flux has a nearly constant distribution over the membrane surface. At this flow rate with a stiffener strand diameter of  $D = 0.1 h$ , a slight improvement in the water flux is observed. As the flow rate is increased, the water flux increases in the regions away from the strands intersections. By comparing Fig. 10 results with the concentration contours in Figs. 6 and 7, it is clear that regions of low water flux coincide with regions of high and low concentration in the feed and draw side of the membrane, respectively. For  $D = 0.2 h$ , the water flux at  $Re = 300$  did increase slightly. For  $Re = 800$ , the distribution became more distinct, and the low water flux regions correspond to low shear stress and high feed concentration. As for  $Re = 1,500$ , a higher value of water flux is observed. Again, the region behind the strand's intersection corresponds to a low water flux region, and it is expected that fouling will be present in these regions. For  $D = 0.3 h$  and  $Re = 300$ , marginal improvement is seen in the water flux. The middle region near the intersection of each strand corresponds to a low water flux region. For  $Re = 800$ , the water flux is increased substantially, and

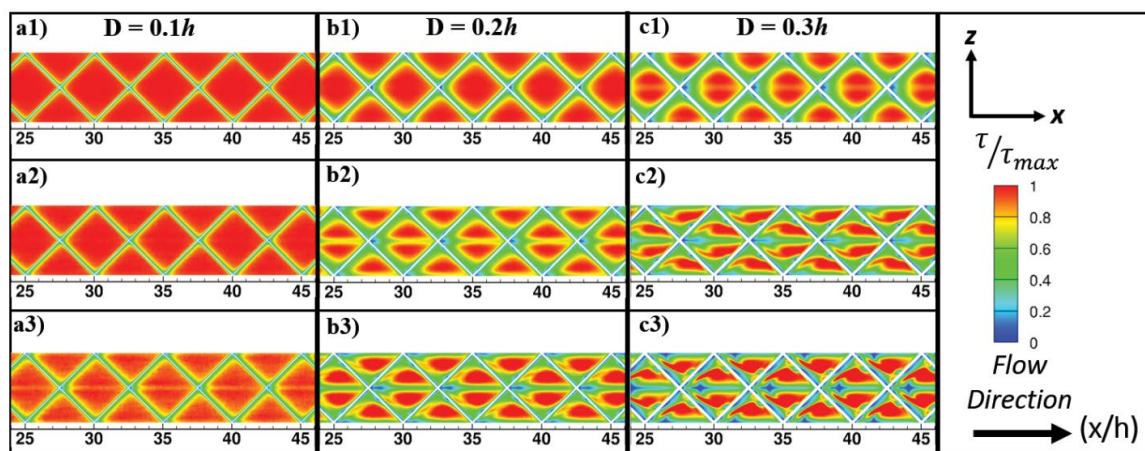


Fig. 9. Normalized shear stress over the membrane surface at the feed side for  $Re = 300$  (a1, b1, c1),  $Re = 800$  (a2, b2, c2), and  $Re = 1,500$  (a3, b3, c3). Flow images are rendered in the module containing membrane with embedded stiffeners of strand diameter  $D = 0.1 h$  (a1, a2, a3),  $D = 0.2 h$  (b1, b2, b3), and  $D = 0.3 h$  (c1, c2, c3).

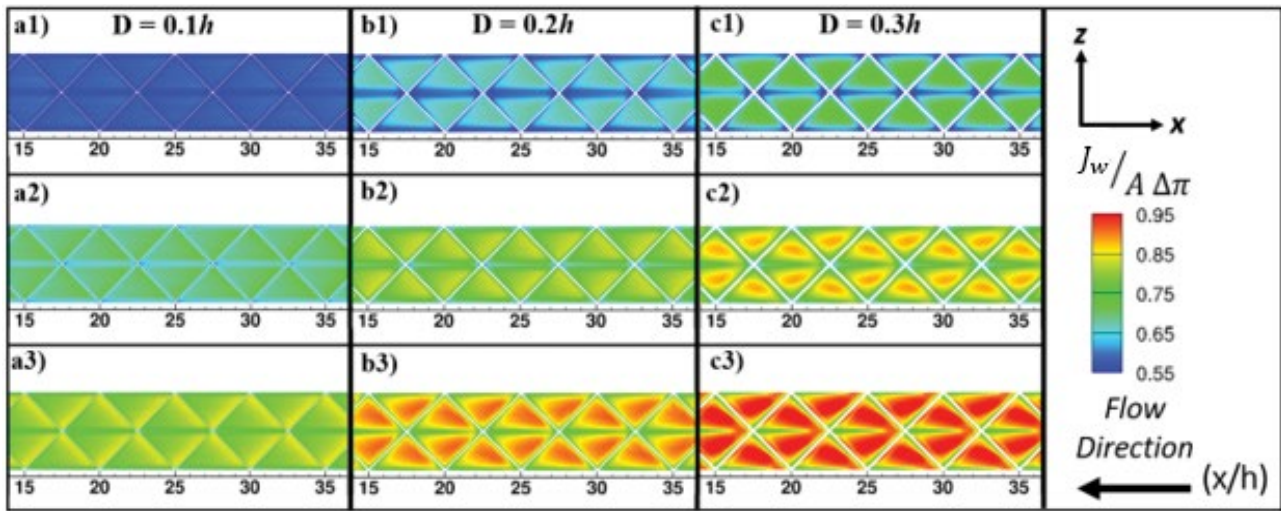


Fig. 10. Normalized water flux for  $Re = 300$  (a1, b1, c1),  $Re = 800$  (a2, b2, c2), and  $Re = 1,500$  (a3, b3, c3). Images are rendered in the module containing membrane with embedded stiffeners of strand diameter  $D = 0.1 h$  (a1, a2, a3),  $D = 0.2 h$  (b1, b2, b3), and  $D = 0.3 h$  (c1, c2, c3).

the low water flux region shrinks in size considerably. A similar trend is seen in  $Re = 1,500$ , with some marginal improvement in the water flux, and the low water flux region started to diminish. Table 4 list the averaged water flux over the membrane surface for all strand’s diameters and flow rates. In each module, the water flux increases as the flow rate is increased. The water flux at any flow rate is increased as the diameter of the stiffener strand increases. The percentage increase in the water permeation rate in the stiffener embedded module compared to the module with flat membrane asymptotes for  $D = 0.3 h$ .

### 3.1. Coefficient of performance

Although the enhancements in the flux performance and the mitigation of concentration polarization are quite good a more detailed quantitative analysis is needed to conclude the better performing modules. Since the introduction of the embedded stiffener will add more friction inside the membrane channels. Therefore, more pumping power is needed to push the feed and draw solution. The coefficient of the performance parameter is used to estimate the overall performance of the module, and it is written as:

Table 4  
Averaged water flux and percentage enhancement for all geometries at all flow rates considered

	Case											
	Flat			$D = 0.1 h$			$D = 0.2 h$			$D = 0.3 h$		
Re	300	800	1,500	300	800	1,500	300	800	1,500	300	800	1,500
Flux ( $\text{kg}/\text{m}^2 \text{h}$ )	50.19	57.93	62.97	55.31	65.45	75.04	60.2	72.70	79.36	63.90	75.16	82.15
Percentage improvement	–	–	–	10.20	12.98	19.17	19.94	25.50	26.03	27.32	29.74	30.46

Table 5  
Module averaged friction factor for the feed and draw stream and the coefficient of performance for all geometries and flow rates considered

Re	Case										
	Empty		$D = 0.1 h$			$D = 0.2 h$			$D = 0.3 h$		
	$f_f$	$f_d$	$f_f$	$f_d$	COP	$f_f$	$f_d$	COP	$f_f$	$f_d$	COP
300	0.26	0.27	0.27	0.28	1.08	0.29	0.30	1.15	0.31	0.32	1.20
800	0.11	0.11	0.12	0.13	1.09	0.13	0.13	1.19	0.15	0.16	1.17
1,500	0.07	0.07	0.08	0.08	1.14	0.09	0.09	1.16	0.12	0.13	1.08

$$\text{COP} = \left( \frac{J_{ws}}{J_{we}} \right) \left( \frac{(f_f + f_d)_e}{(f_f + f_d)_s} \right)^{1/3} \quad (18)$$

where  $J_{ws}$  and  $J_{we}$  are the averaged water flux of the module containing membrane with and without embedded stiffeners, respectively. Also,  $f_f$  and  $f_d$  are the averaged friction factor for the feed and draw channels, respectively. The subscripts  $e$  and  $s$  denote to the module containing membrane without and with embedded stiffeners. The friction factor in either side of the channel is calculated using  $f = 4h \left| \frac{dp}{dx} \right| / (\rho U_{in}^2)$ . Here,  $\left| \frac{dp}{dx} \right|$  is the pressure gradient in the stream-wise

direction. Table 5 lists the friction values in both channels along with the COP for various values of Re and  $D$ . All modules have a COP value of over 1 for the range of flow rate considered in this study. This concludes that the use of embedded stiffeners helps in getting more water flux through the module with no severe penalty of pumping power. The case with  $D = 0.3 h$  and Re = 300 has a COP of 1.20 which is the highest value among all the cases. Whereas the two cases ( $D = 0.1 h$  and Re = 300) and ( $D = 0.3 h$  and Re = 1,500) have a COP 1.08 which is the lowest value attained. Also, for lower flow rates, it is better to use a larger strand diameter while for higher flow rates, the use of smaller strand diameter is recommended. It is important to state again that the fouling is much less likely for  $D = 0.3 h$  and Re = 1,500.

#### 4. Conclusion

This study focusses on characterizing the performance of forward osmosis membrane systems containing membranes with embedded stiffeners. The newly proposed embedded stiffener functions as a mixing tool and support for the membrane, and thus the effect of the porous support layer in the membrane separation process is minimized. A net-type stiffener of 45° was used with three different strand diameters, 0.1, 0.2, and 0.3  $h$ . Results were presented for Reynolds numbers of 300, 800, and 1,500. The separation process in the module containing membranes without embedded stiffeners was simulated for each flow rate as a base case to compare the performance of the embedded stiffener approach. The shear stress transport  $k-\omega$  model was used for the modules with embedded stiffener membrane while a laminar model was employed for the module with a flat membrane. The solution–diffusion model was used to predict the water flux over the membrane surface with no modification since the porous layer effect was neglected. The predicted water and reversed solute flux agree well with measured flux reported by Morrow and Childress [15], validating the mathematical model and numerical method employed in the numerical study. The results show that embedded stiffeners indeed have promoted mixing. Both concentrative and dilutive CP over each side of the membrane were alleviated significantly. Also, the embedded stiffeners increased the shear stress over the membrane surface in the feed side. The increase in the shear stress helps in lowering the chances of fouling over the membrane surface as fouling occurs in regions of low shear stress.

As expected, the highest water flux occurred at  $D = 0.3 h$  and Re = 1,500 (more than 30% increase in the flux), while the lowest water flux occurred at  $D = 0.1 h$  and Re = 300 (still more than 10% increase in the flux). However, a coefficient of performance analysis reveals that the case with  $D = 0.3 h$  and Re = 300 has performed better compared to all the cases. The two cases ( $D = 0.1 h$  and Re = 300) and ( $D = 0.3 h$  and Re = 1,500) had the lowest performance. It is revealed that the embedded membrane with small strand diameter performs better at high flow rates while the membrane with large strand diameter performs better at lower flow rates.

The results show promising performance for the novel embedded-stiffener membrane concept in forward osmosis desalination modules. It is recommended that more study is needed to reach an optimum embedded-stiffener arrangement as there is an endless way of stiffener arrangements.

#### Symbols

$A$	–	Pure water permeability, $m(s \text{ Pa})^{-1}$
$B$	–	Solute permeation coefficient, $m \text{ s}^{-1}$
$C$	–	Solute concentration, $\text{kg m}^{-3}$
$c$	–	Solute mass fraction, $\text{kg}_{\text{solute}} \text{ kg}_{\text{solvent}}^{-1}$
$D_{AB}$	–	Solute diffusion coefficient, $\text{m}^2 \text{ s}^{-1}$
$d_h$	–	Hydraulic diameter, $m$
$\varepsilon$	–	Porous layer porosity, –
$h$	–	Feed and draw channel height, $m$
$J_w$	–	Suction rate, $\text{m}^2 \text{ s}^{-1}$
$J_s$	–	Reverse solute flux, $\text{kg m}^{-2} \text{ s}^{-1}$
$K$	–	Solute resistivity coefficient, $\text{s m}^{-1}$
$\mu$	–	Fluid viscosity, $\text{Pa s}$
$p$	–	Pressure, $\text{Pa}$
$\pi$	–	Osmotic pressure coefficient, $\text{Pa}$
Re	–	Reynolds number, –
$t_s$	–	Porous layer thickness, $m$
$\tau$	–	Tortuosity of porous layer, –
$\rho$	–	Density of fluid, $\text{kg m}^{-3}$
$U$	–	Velocity vector, $\text{m s}^{-1}$
$\bar{u}$	–	Average inlet velocity, $\text{m s}^{-1}$
$x y z$	–	Cartesian coordinates, $m$

#### Subscripts

dB	–	Draw bulk
fB	–	Feed bulk
$f$	–	Feed solution
$d$	–	Draw solution
$c$	–	Corrugation
$e$	–	Flat channel

#### Acknowledgments

This work used Extreme Science and Engineering Discovery Environment (XSEDE) for running all the CFD simulations, which is supported by the National Science Foundation grant number TG-CT170051. This work used the Bridges system at the Pittsburgh Supercomputing Center (PSC).

#### References

- [1] M. Qasim, N.A. Darwish, S. Sarp, N. Hilal, Water desalination by forward (direct) osmosis phenomenon: a comprehensive review, *Desalination*, 374 (2015) 47–69.

- [2] R. Valladares Linares, Z. Li, S. Sarp, S.S. Bucs, G. Amy, J.S. Vrouwenvelder, Forward osmosis niches in seawater desalination and wastewater reuse, *Water Res.*, 66 (2014) 122–139.
- [3] F.A. Siddiqui, Q. She, A.G. Fane, R.W. Field, Exploring the differences between forward osmosis and reverse osmosis fouling, *J. Membr. Sci.*, 565 (2018) 241–253.
- [4] X. Song, Z. Liu, D.D. Sun, Nano gives the answer: breaking the bottleneck of internal concentration polarization with a nanofiber composite forward osmosis membrane for a high water production rate, *Adv. Mater.*, 23 (2011) 3256–3260.
- [5] H.Q. Liang, W.S. Hung, H.H. Yu, C.C. Hu, K.R. Lee, J.Y. Lai, Z.K. Xu, Forward osmosis membranes with unprecedented water flux, *J. Membr. Sci.*, 529 (2017) 47–54.
- [6] R.M. El Khaldi, M.E. Pasaoglu, S. Guclu, Y.Z. Menceloglu, R. Ozdogan, M. Celebi, M.A. Kaya, I. Koyuncu, Fabrication of high-performance nanofiber-based FO membrane, *Desal. Water Treat.*, 147 (2019) 56–72.
- [7] J. Marc, C. Puguán, H. Kim, K. Lee, H. Kim, Low internal concentration polarization in forward osmosis membranes with hydrophilic crosslinked PVA nano fibers as porous support layer, *Desalination*, 336 (2014) 24–31.
- [8] M. Ghanbari, D. Emadzadeh, W.J. Lau, H. Riazi, D. Almasi, A.F. Ismail, Minimizing structural parameter of thin film composite forward osmosis membranes using polysulfone/halloysite nanotubes as membrane substrates, *Desalination*, 377 (2016) 152–162.
- [9] W. Kuang, Z. Liu, H. Yu, G. Kang, X. Jie, Y. Jin, Y. Cao, Investigation of internal concentration polarization reduction in forward osmosis membrane using nano-CaCO<sub>3</sub> particles as sacrificial component, *J. Membr. Sci.*, 497 (2016) 485–493.
- [10] N. Bui, J.R. Mccutcheon, Nanoparticle-embedded nano fibers in highly permselective thin-film nanocomposite membranes for forward osmosis, *J. Membr. Sci.*, 518 (2016) 338–346.
- [11] M. Zheng, X. Zhao, S. Xu, D. Lu, Ultrathin support-free membrane with high water flux for forward osmosis desalination, *Water Air Soil Pollut.*, 230 (2019), doi: 10.1007/s11270-019-4192-z.
- [12] M. Li, V. Karanikola, X. Zhang, L. Wang, M. Elimelech, A self-standing, support-free membrane for forward osmosis with no internal concentration polarization, *Environ. Sci. Technol. Lett.*, 5 (2018) 266–271.
- [13] A.H. Hawari, A. Al-Qahoumi, A. Ltaief, S. Zaidi, A. Altaee, Dilution of seawater using dewatered construction water in a hybrid forward osmosis system, *J. Cleaner Prod.*, 195 (2018) 365–373.
- [14] S. Moulik, P. Vadthya, Y.R. Kalipatnapu, S. Chenna, S. Sundergopal, Production of fructose sugar from aqueous solutions: nanofiltration performance and hydrodynamic analysis, *J. Cleaner Prod.*, 92 (2015) 44–53.
- [15] C. Morrow, A. Childress, Evidence, determination, and implications of membrane-independent limiting flux in forward osmosis systems, *Environ. Sci. Technol.*, 53 (2019) 4380–4388.
- [16] A.M. Alshwairekh, A. Alghafis, A.M. Alwatban, U.F. Algasair, A. Oztekin, The effect of membrane and channel corrugation in forward osmosis membrane modules – numerical analyses, *Desalination*, 460 (2019) 41–55.
- [17] V. Geraldes, V. Semião, M.N. De Pinho, Flow and mass transfer modelling of nanofiltration, *J. Membr. Sci.*, 191 (2001) 109–128.
- [18] A.E. Anqi, N. Alkhamis, A. Oztekin, Numerical simulation of brackish water desalination by a reverse osmosis membrane, *Desalination*, 369 (2015) 156–164.
- [19] A.E. Anqi, N. Alkhamis, A. Oztekin, Computational study of desalination by reverse osmosis – three-dimensional analyses, *Desalination*, 388 (2016) 38–49.
- [20] A.E. Anqi, N. Alkhamis, A. Oztekin, Steady three dimensional flow and mass transfer analyses for brackish water desalination by reverse osmosis membranes, *Int. J. Heat Mass Transfer*, 101 (2016) 399–411.
- [21] M. Usta, A.E. Anqi, A. Oztekin, Reverse osmosis desalination modules containing corrugated membranes – computational study, *Desalination*, 416 (2017) 129–139.
- [22] M. Alrehili, M. Usta, N. Alkhamis, A.E. Anqi, A. Oztekin, Flows past arrays of hollow fiber membranes – gas separation, *Int. J. Heat Mass Transfer*, 97 (2016) 400–411.
- [23] L.-Z. Zhang, Convective mass transport in cross-corrugated membrane exchangers, *J. Membr. Sci.*, 260 (2005) 75–83.
- [24] L. Zhang, Z. Chen, Convective heat transfer in cross-corrugated triangular ducts under uniform heat flux boundary conditions, *Int. J. Heat Mass Transfer*, 54 (2011) 597–605.
- [25] I.S. Kang, H.N. Chang, The effect of turbulence promoters on mass transfer – numerical analysis and flow visualization, *Int. J. Heat Mass Transfer*, 25 (1982) 1167–1181.
- [26] F.R. Menter, Two-equation eddy-viscosity turbulence models for engineering applications, *AIAA J.*, 32 (1994) 1598–1605.
- [27] J.A. Baker, Membrane technology and applications, *Q. Rev. Biol.*, 79 (2004) 443.
- [28] L. Xia, M.F. Andersen, C. He, R. Mccutcheon, Novel commercial aquaporin flat-sheet membrane for forward osmosis, 56 (2017) 11919–11925.
- [29] M.F. Gruber, C.J. Johnson, C.Y. Tang, M.H. Jensen, L. Yde, C. Hélix-Nielsen, Computational fluid dynamics simulations of flow and concentration polarization in forward osmosis membrane systems, *J. Membr. Sci.*, 379 (2011) 488–495.
- [30] S. Wardeh, H.P. Morvan, CFD simulations of flow and concentration polarization in spacer-filled channels for application to water desalination, *Chem. Eng. Res. Des.*, 86 (2008) 1107–1116.
- [31] N. Akther, S. Daer, S.W. Hasan, Effect of flow rate, draw solution concentration and temperature on the performance of TFC FO membrane, and the potential use of ro reject brine as a draw solution in FO-RO hybrid systems, *Desal. Water Treat.*, 136 (2018) 65–71.